ASME Journal of Vibration and Acoustics
Online journal at:
https://asmedigitalcollection.asme.org/vibrationacoustics

Chengyun Du
Thrust of Internet of Things,
The Hong Kong University of Science and Technology (Guangzhou),
Guangzhou, Guangdong 511400, China
e-mail: chengyun_du@163.com

Shuai Jiang
Thrust of Internet of Things,
The Hong Kong University of Science and Technology (Guangzhou),
Guangzhou, Guangdong 511400, China
e-mail: js1736957811@126.com

Shuai Qu
College of Transportation,
Tongji University,
Shanghai 201804, China
e-mail: shuaiqu@tongji.edu.cn

Xiao Wang
National Key Laboratory of Helicopter Aeromechanics,
Nanjing University of Aeronautics and Astronautics,
Nanjing, Jiangsu 210016, China
e-mail: x.wang@nuaa.edu.cn

Yingqi Zhang
China Helicopter Research and Development Institute,
Jingdezhen, Jiangxi 333001, China
e-mail: 2867092484@qq.com

Chunbo Lan
National Key Laboratory of Helicopter Aeromechanics,
Nanjing University of Aeronautics and Astronautics,
Nanjing, Jiangsu 210016, China
e-mail: chunbolan@nuaa.edu.cn

Guobiao Hu[1]
Thrust of Internet of Things,
The Hong Kong University of Science and Technology (Guangzhou),
Guangzhou, Guangdong 511400, China
e-mail: guobiaohu@hkust-gz.edu.cn

Vehicle-Level Modeling and Analysis of Onboard Energy Harvesters and Their Impact on Dynamics

Integrating energy harvesters into rail transit systems, such as vehicles, offers a sustainable power solution for onboard sensors, yet their impact on vehicle dynamics remains largely underexplored. This study proposes an approach that combines vehicle dynamics, energy harvesters, and interface circuits to thoroughly analyze bidirectional complex coupling effects between the subsystems. An equivalent circuit model (ECM) is developed by employing the mechanical-electrical analogy theory to simulate vehicle dynamics, and its accuracy is verified through comparison with a traditional dynamic model. Subsequently, electromagnetic and piezoelectric harvesters were integrated into the model, along with power-boosting interface circuits, to assess the combined effects. The energy-harvesting performance and the vehicle dynamic behaviors under harmonic and random excitations were investigated. Results indicated that the power-boosting interface circuits can significantly enhance energy harvesting efficiency and stabilize power output under different excitation conditions. However, the installation of energy harvesters deteriorates vehicle dynamics noticeably, and the power-boosting interface circuits further exacerbate these effects, particularly at low frequencies. In general, the proposed ECM presents a comprehensive method for the design and optimization of onboard energy harvesters and their interface circuits, offering insights from a system-level analysis for rail transit applications.
[DOI: 10.1115/1.4069337]

Keywords: vehicle dynamics, onboard energy harvester, interface circuit, equivalent circuit model, mechatronics and electromechanical systems, smart materials and structures

1 Introduction

With the rapid advancement of rail transit technology, train-track systems have become increasingly intelligent and digitalized. Sensors embedded within both vehicles and track systems play a

[1]Corresponding author.
Contributed by the Technical Committee on Vibration and Sound of ASME for publication in the Journal of Vibration and Acoustics. Manuscript received March 28, 2025; final manuscript received July 30, 2025; published online August 20, 2025. Assoc. Editor: Shahrzad Towfighian.

vital role in ensuring operational safety, enhancing passenger comfort, and optimizing operational efficiency [1–5] by monitoring the health conditions of bridges [6–8], tracks [9,10], and various vehicle components [2,11,12]. Onboard sensors require a stable power supply to function reliably. However, traditional battery-powered methods suffer from short lifespans and high maintenance costs, making them unsuitable to meet the efficiency and low-maintenance demands of modern rail transit [13]. Vibration energy harvesting has emerged as a promising alternative to batteries in specific applications. In rail transit, where vibrations are abundant, this approach is particularly advantageous. Well-designed onboard energy harvesters are expected to harness mechanical energy generated during vehicle operation and convert it into electrical energy, offering a green and sustainable energy solution for onboard sensors [14].

Existing onboard energy harvesters can be primarily categorized into two types [3,15]: electromagnetic energy harvesters (EMEH) and piezoelectric energy harvesters (PEH). EMEHs generate electrical by converting kinetic motion into electromagnetic induction, utilizing the relative movement between different vehicle components [16,17]. To improve transmission durability and efficiency, Liu et al. [18] developed an innovative energy harvester incorporating a ball-screw mechanism and one-way clutches to implement a mechanical motion rectifier. Their design converts bidirectional suspension vibrations into unidirectional generator rotation, effectively mitigating the operational instability caused by bidirectional vibrations in the suspension system. In field tests, it produced an average power of 13.3 W and reduced chassis acceleration by 11.12%, demonstrating superior mechanical efficiency and reduced backlash compared to traditional designs. Pan et al. [13] proposed a similar design and considered the effect of harvester installation on the vehicle. In the in-lab test at 90 km/h, the harvester generated an average power of 14.5 W, and the field test at 30 km/h produced 1.3 W.

Unlike electromagnetic energy harvesters, piezoelectric energy harvesters operate on a different principle, leveraging the piezoelectric effect to convert mechanical energy into electrical energy [19,20]. To enhance their energy conversion efficiency, researchers have developed various PEH designs. For instance, Wang et al. [21] developed a T-shaped PEH with hybrid nonlinearity capable of operating within the range of 1–11 Hz under an excitation of 0.5 g. It delivers a peak power of 605 μW to power wireless sensors and maintains stable output for over 121 h after being installed in a freight train's axle box. Lopes et al. [22] optimized the geometries of planar zigzag (PZ) and orthogonal spiral outer (OSo) to maximize power generation while minimizing the weight of multibeam PEHs. Among the solutions, the OSo configuration achieved a maximum output power of 20.93 mW, while the PZ design attained the highest energy density of 16.595 mW/kg, both capable of powering typical onboard devices. Despite significant advancements in energy-harvesting research, their power outputs in real-world operating conditions are often significantly affected by factors such as load frequency and external loads due to the complexity of the vehicle operating environment. As a result, further optimization is needed to improve their stability and efficiency [23].

As electromechanically coupled systems, energy harvesters require performance enhancements through both mechanical structure optimization and advancements in circuit design. Synchronized electric charge extraction (SECE) [24–26] and synchronized magnetic flux extraction (SMFE) circuits [16,27–30] are two typical shunt circuits designed for piezoelectric energy harvesters and electromagnetic energy harvesters, respectively. Lefeuvre et al. [24] first introduced the SECE circuit to optimize the energy flow in PEH devices. By implementing a specialized synchronization method for charge extraction, the harvested power increased by 400% in the experiment. Expanding on a similar yet different principle, Arroyo and Badel [27] developed a new extraction technique, SMFE, for EMEHs. Compared with conventional methods, the SMFE circuit can harvest 2.5 times more power. These two circuits can not only enhance energy-harvesting efficiency but also address the impedance matching issues [27,28]. However, while interface circuits can improve the performance of harvesters, their installation may also impact vehicle dynamics [13,31]. This is because integrating interface circuits alters the coupling behavior between the harvester and the vehicle, affecting the vehicle's overall dynamic response. Therefore, studying these coupling effects requires treating the vehicle, harvester, and interface circuit as a unified system.

Several studies have investigated the coupled dynamics between vehicles and energy harvesters, as well as between tracks and energy harvesters. Pan et al. [31] modeled their onboard energy harvester as an equivalent damping and mass unit and examined the influence of its installation locations on vehicle ride comfort. Their results showed that when the equivalent mass exceeds 1400 kg, placing energy harvesters at the front and rear ends of the vehicle can reduce ride comfort. Du et al. [32] modeled a piezoelectric stack energy harvester installed beneath the floating plate as an equivalent spring. By analyzing the impact of its equivalent stiffness on the dynamic behavior of the floating slab track, they identified an optimal stiffness range that ensures track safety. Within this range, two novel designs were proposed to enhance energy conversion efficiency. However, previous studies have primarily analyzed vehicle dynamics and energy harvesters separately, often overlooking the interactions between them [13,33]. While this approach simplifies the analysis, it fails to fully capture the true impact of both the harvester and interface circuits on vehicle dynamics. In fact, the vehicle's dynamic behavior directly determines the mechanical input/excitation to the harvester, thus affecting its electrical output. Conversely, the energy-harvesting process influences vehicle dynamics through electromechanical interactions, resulting in a complex bidirectional coupling. Therefore, accurately assessing the effects of harvesters and interface circuits on the overall vehicle system necessitates an integrated modeling and analysis approach that treats the vehicle, the energy harvester, and the interface circuit as a unified system.

Building on this understanding, this study first applied electromechanical analogy theory to establish an equivalent circuit model for traditional vertical vehicle dynamic systems. In addition, an integrated model comprising the vehicle, energy harvester, and interface circuit has also been developed. This model provides a unified representation of the mechanical and electrical systems while preserving their physical significance, thus facilitating the simulation and analysis of the entire system. Based on this model, the study further examines the impact of interface circuits under various load conditions, including harmonic and random loads, on both the energy harvester's power output and the vehicle's dynamic response. The results indicate that incorporating interface circuits, such as the SMFE and SECE circuits, can significantly enhance the power output and stability of the energy harvester. However, they may also further accentuate variations in vehicle dynamics. Therefore, in practical applications, interface circuit design should fully consider the vehicle's operating environment and the sensors' power demands to achieve an optimal balance between energy efficiency and system stability.

2 Theoretical Models of the Subsystems

The typical installation location for onboard energy harvesters is between the car body and the bogies, operating in parallel with the secondary suspension [12,13,31,34]. By harnessing the vibration of the secondary suspension, the harvester effectively converts mechanical energy into electrical energy, providing a reliable power source for onboard sensors. The dynamic model of the vehicle integrated with harvesters in the secondary suspension is shown in Fig. 1, where the vehicle is simplified and represented as a 10-degree-of-freedom (DOF) system. The two energy harvesters are installed: one at the front suspension between the front bogie frame and the car body, and the other at the rear suspension between the rear bogie frame and the car body. As the vehicle moves, track

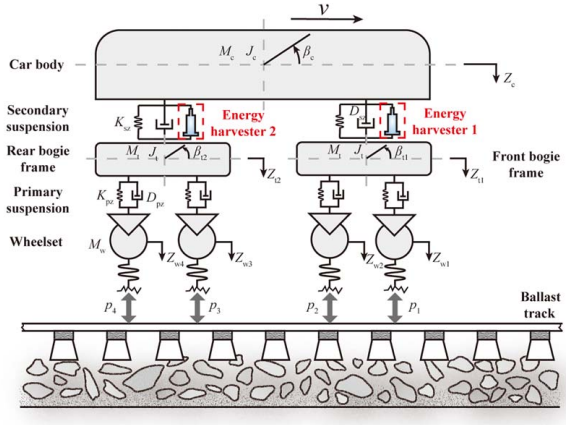

Fig. 1 The dynamic model of the vehicle integrated with onboard energy harvesters in the secondary suspension system

irregularities induce vibrations and cause relative displacement between the car body and bogies, providing the harvesters with the opportunity to generate electricity through their internal components. At the same time, the harvesters generate a reaction force, F_{EH}, which influences the vehicle dynamics.

Using D'Alembert's principle, the vibration equations for the vehicle system with installed energy harvesters can be derived as follows:

- Vertical motion of the car body

$$\begin{pmatrix} M_c\ddot{Z}_c + 2D_{sz}\dot{Z}_c + 2K_{sz}Z_c - D_{sz}\dot{Z}_{t1} - \\ K_{sz}Z_{t1} - D_{sz}\dot{Z}_{t2} - K_{sz}Z_{t2} + F_{EH1} + F_{EH2} \end{pmatrix} = M_c g \quad (1)$$

- Pitch motion of the car body

$$\begin{pmatrix} J_c\ddot{\beta}_c + 2D_{sz}l_c^2\dot{\beta}_c + 2K_{sz}l_c^2\beta_c + D_{sz}l_c\dot{Z}_{t1} - D_{sz}l_c\dot{Z}_{t2} \\ +K_{sz}l_cZ_{t1} - K_{sz}l_cZ_{t2} - F_{EH1}l_c + F_{EH2}l_c \end{pmatrix} = 0 \quad (2)$$

- Vertical motion of the front bogie frame

$$\begin{aligned} M_t\ddot{Z}_{t1} + (2D_{pz} + D_{sz})\dot{Z}_{t1} + (2K_{pz} + K_{sz})Z_{t1} - D_{sz}\dot{Z}_c - K_{sz}Z_c \\ - D_{pz}\dot{Z}_{w1} - D_{pz}\dot{Z}_{w2} - K_{pz}Z_{w1} - K_{pz}Z_{w2} + D_{sz}l_c\dot{\beta}_c \\ + K_{sz}l_c\beta_c - F_{EH1} = M_t g \end{aligned} \quad (3)$$

- Pitch motion of the front bogie frame

$$\begin{aligned} J_t\ddot{\beta}_{t1} + 2D_{pz}l_t^2\dot{\beta}_{t1} + 2K_{pz}l_t^2\beta_{t1} + D_{pz}l_t\dot{Z}_{w1} - D_{pz}l_t\dot{Z}_{w2} \\ + K_{pz}l_tZ_{w1} - K_{pz}l_tZ_{w2} = 0 \end{aligned} \quad (4)$$

- Vertical motion of the rear bogie frame

$$\begin{aligned} M_t\ddot{Z}_{t2} + (2D_{pz} + D_{sz})\dot{Z}_{t2} + (2K_{pz} + K_{sz})Z_{t2} - D_{sz}\dot{Z}_c - K_{sz}Z_c \\ - D_{pz}\dot{Z}_{w3} - D_{pz}\dot{Z}_{w4} - K_{pz}Z_{w3} - K_{pz}Z_{w4} - D_{sz}l_c\dot{\beta}_c \\ - K_{sz}l_c\beta_c - F_{EH2} = M_t g \end{aligned} \quad (5)$$

- Pitch motion of the rear bogie frame

$$\begin{aligned} J_t\ddot{\beta}_{t2} + 2D_{pz}l_t^2\dot{\beta}_{t2} + 2K_{pz}l_t^2\beta_{t2} + D_{pz}l_t\dot{Z}_{w3} - D_{pz}l_t\dot{Z}_{w4} \\ + K_{pz}l_tZ_{w3} - K_{pz}l_tZ_{w4} = 0 \end{aligned} \quad (6)$$

- Vertical motion of the first wheelset

$$\begin{aligned} M_w\ddot{Z}_{w1} + D_{pz}\dot{Z}_{w1} + K_{pz}Z_{w1} - D_{pz}\dot{Z}_{t1} - K_{pz}Z_{t1} + D_{pz}l_t\dot{\beta}_{t1} \\ + K_{pz}l_t\beta_{t1} + 2p_1(t) - M_w g = F_{01}(t) \end{aligned} \quad (7)$$

- Vertical motion of the second wheelset

$$\begin{aligned} M_w\ddot{Z}_{w2} + D_{pz}\dot{Z}_{w2} + K_{pz}Z_{w2} - D_{pz}\dot{Z}_{t1} - K_{pz}Z_{t1} - D_{pz}l_t\dot{\beta}_{t1} \\ - K_{pz}l_t\beta_{t1} + 2p_2(t) - M_w g = F_{02}(t) \end{aligned} \quad (8)$$

- Vertical motion of the third wheelset

$$\begin{aligned} M_w\ddot{Z}_{w3} + D_{pz}\dot{Z}_{w3} + K_{pz}Z_{w3} - D_{pz}\dot{Z}_{t2} - K_{pz}Z_{t2} + D_{pz}l_t\dot{\beta}_{t2} \\ + K_{pz}l_t\beta_{t2} + 2p_3(t) - M_w g = F_{03}(t) \end{aligned} \quad (9)$$

- Vertical motion of the fourth wheelset

$$\begin{aligned} M_w\ddot{Z}_{w4} + D_{pz}\dot{Z}_{w4} + K_{pz}Z_{w4} - D_{pz}\dot{Z}_{t2} - K_{pz}Z_{t2} - D_{pz}l_t\dot{\beta}_{t2} \\ - K_{pz}l_t\beta_{t2} + 2p_4(t) - M_w g = F_{04}(t) \end{aligned} \quad (10)$$

F_{EH1} and F_{EH2} represent the reaction forces generated by the energy harvesters installed on the front and rear bogies, respectively. The definitions of the parameters in the equations can be found in the Nomenclature.

The two common types of energy harvesters are electromagnetic energy harvesters (EMEHs) and piezoelectric energy harvesters (PEHs). Although conventional piezoelectric materials are known for their brittleness, recent advancements have led to the development of more robust alternatives, such as macro-fiber composites. These technologies offer enhanced mechanical compliance and are better suited for dynamic and harsh environments, including railway systems. Moreover, ongoing research in material science continues to improve the durability of piezoelectric materials, potentially addressing brittleness issues in future applications. Several studies have already explored the feasibility of using piezoelectric transducers for energy harvesting in railway systems, supporting their practical implementation in such settings [21,35], often implemented in cantilever beam configurations [19,33]. In addition, hybrid designs that combine piezoelectric and electromagnetic transductions have been proposed [36,37], resulting in improved mechanical robustness and higher power output. Therefore, it is necessary to investigate both piezoelectric energy harvesters and electromagnetic energy harvesters to advance the development of practical and efficient onboard energy-harvesting systems. Figure 2(*a*) shows the schematic of a general EMEH attached to a target structure, represented as a 1-DOF oscillator by lumped parameters. The EMEH can be shunted to an arbitrary interface circuit, often simplified as a pure resistor in previous studies. Similarly, Fig. 2(*b*) illustrates the general installation of a PEH connected to an interface circuit. The performance of both types of harvesters can be enhanced through rational structural design and optimization of interface circuits.

During vehicle operation, energy harvesters convert mechanical energy in the form of vibrations into electrical energy [24,27]. However, the electromagnetic and piezoelectric transduction mechanisms exhibit distinct electromechanical coupling characteristics. For the EMEH, the electromechanical coupling equation can be written as follows:

$$\begin{cases} M\ddot{x} + D\dot{x} + Kx + \alpha I = M\ddot{y} \\ V + L\dot{I} + RI = \alpha\dot{x} \end{cases} \quad (11)$$

In Eq. (11), V and I represent the voltage and current generated by the EMEH, R denotes the external load resistance, and α is the electromechanical coupling coefficient of the EMEH. This coupling coefficient depends on the magnetic flux density, the coil design, and the geometry and configuration of the components of the EMEH [27]. Under these conditions, the reaction force generated by the EMEH is calculated as $F_{EH} = \alpha I$.

Similarly, the governing equations for a general PEH are given in Eq. (12), where β represents its electromechanical coupling

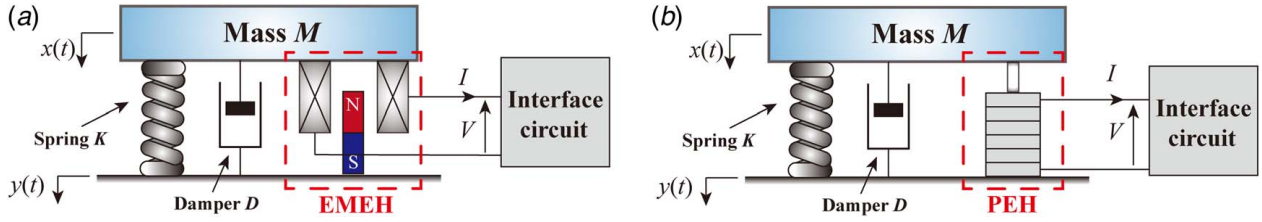

Fig. 2 Equivalent lumped models of a general (*a*) EMEH and (*b*) PEH attached to a target structure, i.e., the secondary suspension system in this study

coefficient. In this case, the reaction force is expressed as $F_{EH} = \beta V$:

$$\begin{cases} M\ddot{x} + D\dot{x} + Kx + \beta V = M\ddot{y} \\ \dfrac{V}{R} + C\dot{V} = \beta\dot{x} \end{cases} \tag{12}$$

A comparison of Eqs. (11) and (12) reveals that electromechanical coupling in the EMEH is based on current and velocity, whereas in the PEH, it depends on voltage and velocity. Therefore, when modeling the electromechanical coupling effects between the vehicle and the energy harvester in an equivalent circuit, different conversion circuits are required for the two different types of harvesters [24,27].

As mentioned before, enhancing the outputs of energy harvesters can be achieved not only through structural optimization but also by utilizing advanced power-boosting interface circuits [16,25–27]. The SMFE and SECE are two widely used circuits, with their schematic diagrams shown in Fig. 3.

The SMFE circuit, as shown in Fig. 3(*a*), consists of two diodes, two capacitors, and a switch. It was originally developed to boost the power output of an EMEH, which is simplified as a voltage source in the figure to highlight the topology of the SMFE circuit. The switch remains closed before the current I_1 reaches its peak. When the current I_1 reaches its peak, the switch S_1 immediately opens, instantaneously transferring the energy stored in the inductor to the storage capacitor. This sudden, instant transition results in significantly high voltage and current. Once the energy transfer is complete, the switch closes again, completing one cycle [16]. The SECE circuit for a PEH, as shown in Fig. 3(*b*), adopts a different topology. To highlight the SECE circuit, the PEH is represented as a current source. The switch S_1 remains open before the voltage V_1 across the piezoelectric transducer reaches its peak. When the voltage V_1 reaches its peak, the switch S_1 immediately closes, transferring the energy stored in capacitor C_1 to inductor L_1. After the first-stage transfer, the switch reopens, and the energy transferred to L_1 starts to charge capacitor C_2, marking the second-stage transfer. This process repeats cyclically. Extensive studies have proven that both circuits can effectively enhance energy conversion efficiency and boost power output. Moreover, they can resolve resistance-matching issues [27,28].

3 Equivalent Circuit Model of the Coupled System

In practical applications, the vehicle, energy harvester, and interface circuit form a fully integrated system with complex interactions. However, as this system comprises both mechanical and electrical subsystems, previous studies have often analyzed them separately, neglecting the bidirectional coupling effects for simplicity. In this study, to thoroughly investigate the coupling effects and accurately model the overall dynamics, we develop an equivalent circuit model (ECM) for the vehicle based on the mechanical–electrical analogy theory, implemented in SIMETRIX software, as shown in Fig. 4.

The vehicle shown in Fig. 1 is represented by seven mass blocks interconnected by six stiffness-damping units. By reformulating Eqs. (1)–(10) as circuit equations while preserving their mathematical integrity, the ECM of the vehicle can then be established. The correspondences between the electrical and mechanical quantities of the vehicle are detailed in Table 1. The established ECM of the vehicle comprises 7 voltage sources, 10 inductors, 12 resistances, and 12 capacitors. Notably, the number of components in the ECM of the vehicle differs from that in its original model. This discrepancy arises because some mechanical components have multiple DOFs, each of which requires a separate governing equation to describe. Since the ECM is inherently derived from these equations, the number of circuit loops in the ECM corresponds to the number of governing equations rather than the number of mechanical components. For instance, to be more specific, the mass blocks exhibit both vertical and pitch motion. Since the inductors correspond to these mass blocks, they should be present in both the vertical displacement and pitch motion loops. However, connecting them to both loops would result in a short circuit. To resolve this issue, nonlinear transfer function modules provided in SIMETRIX are utilized to create separate loops while sharing a single inductor.

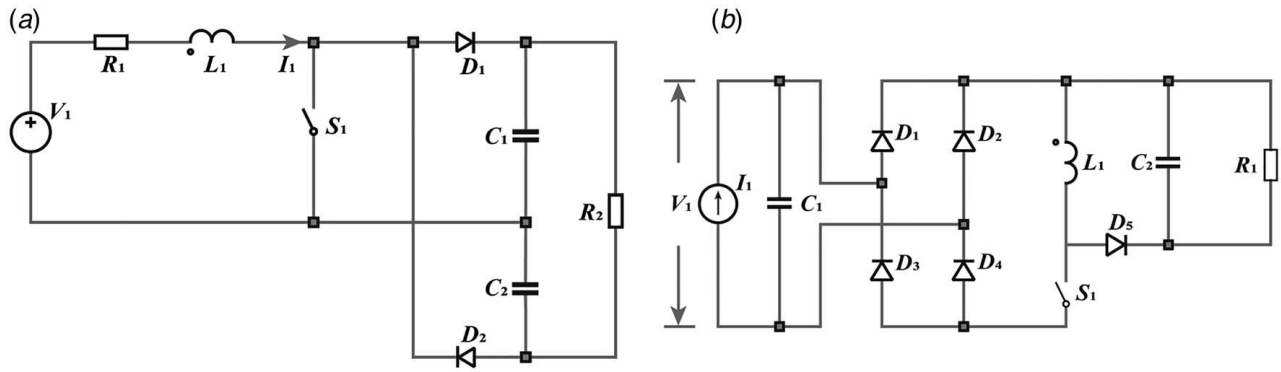

Fig. 3 Schematic diagrams of (*a*) SMFE and (*b*) SECE interface circuits

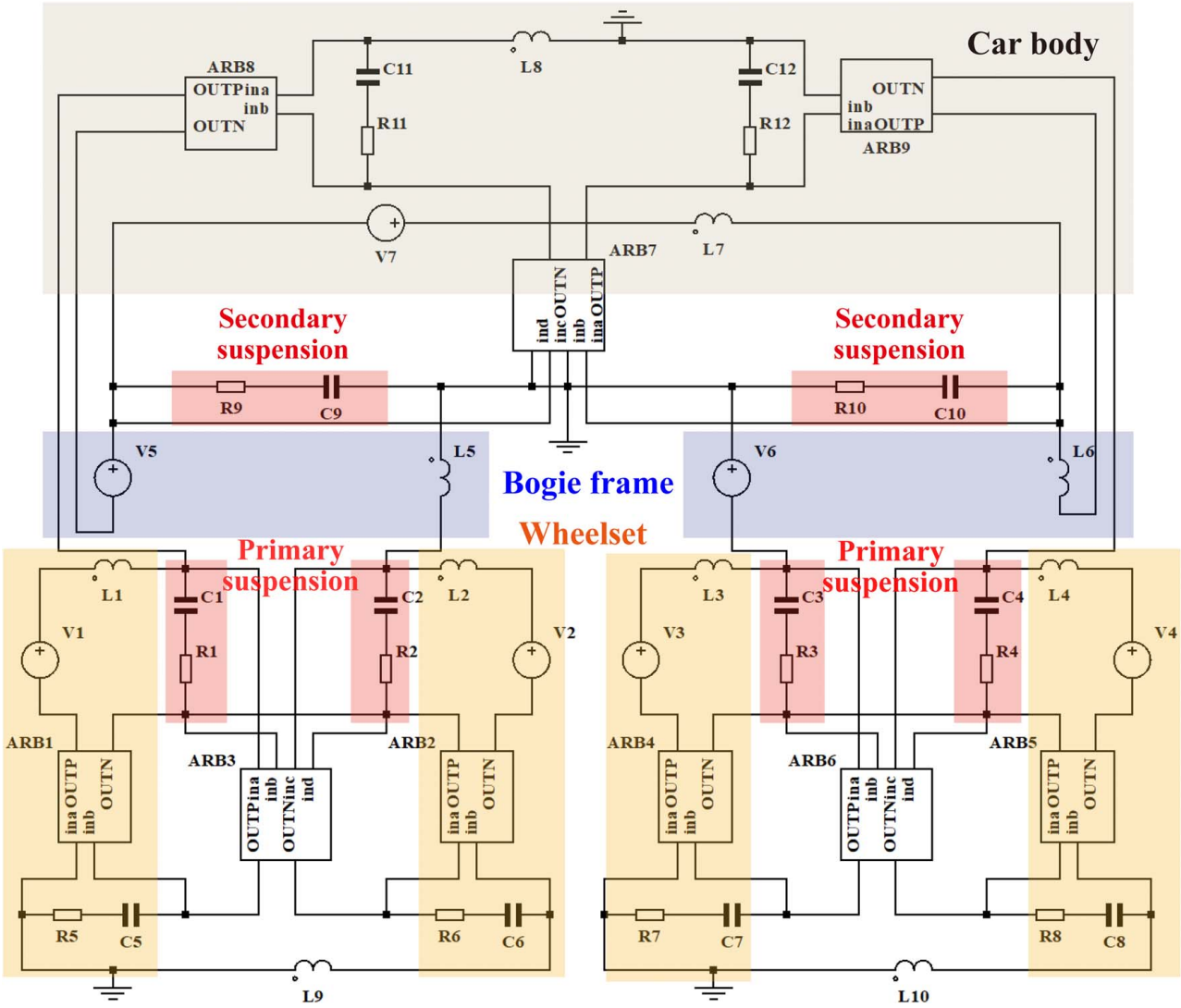

Fig. 4 Equivalent circuit model of the vehicle dynamic model

Table 1 Analogous parameters between the mechanical domain and electrical domain [38]

Mechanical parameters			Equivalent circuit parameters		Value
Mass	Mass of wheelset	M_w	Inductance	L_1–L_4	1350 H
	Mass of bogie	M_t		L_5 and L_6	2980 H
	Mass of car body	M_c		L_7	38,500 H
Moment of inertia	Vehicle roll moment of inertia	J_c		L_8	3.47×10^4 H
	Bogie roll moment of inertia	J_t		L_9 and L_{10}	2503 H
Damping	Primary suspension vertical damping	D_{pz}	Resistance	R_1–R_8	4.9×10^4 Ω
	Secondary suspension vertical damping	D_{sz}		R_9–R_{12}	1.96×10^5 Ω
Reciprocal of stiffness	Primary suspension vertical damping	$1/K_{pz}$	Capacitance	C_1–C_8	4.67×10^{-7} F
	Secondary suspension vertical damping	$1/K_{sz}$		C_9–C_{12}	3.95×10^{-7} F

Table 2 Parameters of the vehicle system [38]

Parameters	Values	Parameters	Values
Mass of car body, M_c	38,500 kg	Secondary vertical stiffness, K_{sz}	2.535×10^6 N/m
Mass of bogie, M_t	2980 kg	Primary vertical damping, D_{pz}	4.9×10^4 (N·s)/m
Mass of wheelset, M_w	1350 kg	Secondary vertical damping, D_{sz}	1.96×10^5 (N·s)/m
Vehicle speed, v	140 km/h	Half of rolling stock axle spacing, l_c	8.4 m
Vehicle roll moment of inertia, J_c	2.446×10^6 kg·m^2	Half of wheel base, l_t	1.2 m
Bogie roll moment of inertia, J_t	3605 kg·m^2	Nominal wheel radius, R_r	0.4575 m
Primary vertical stiffness, K_{pz}	2.14×10^6 N/m	–	–

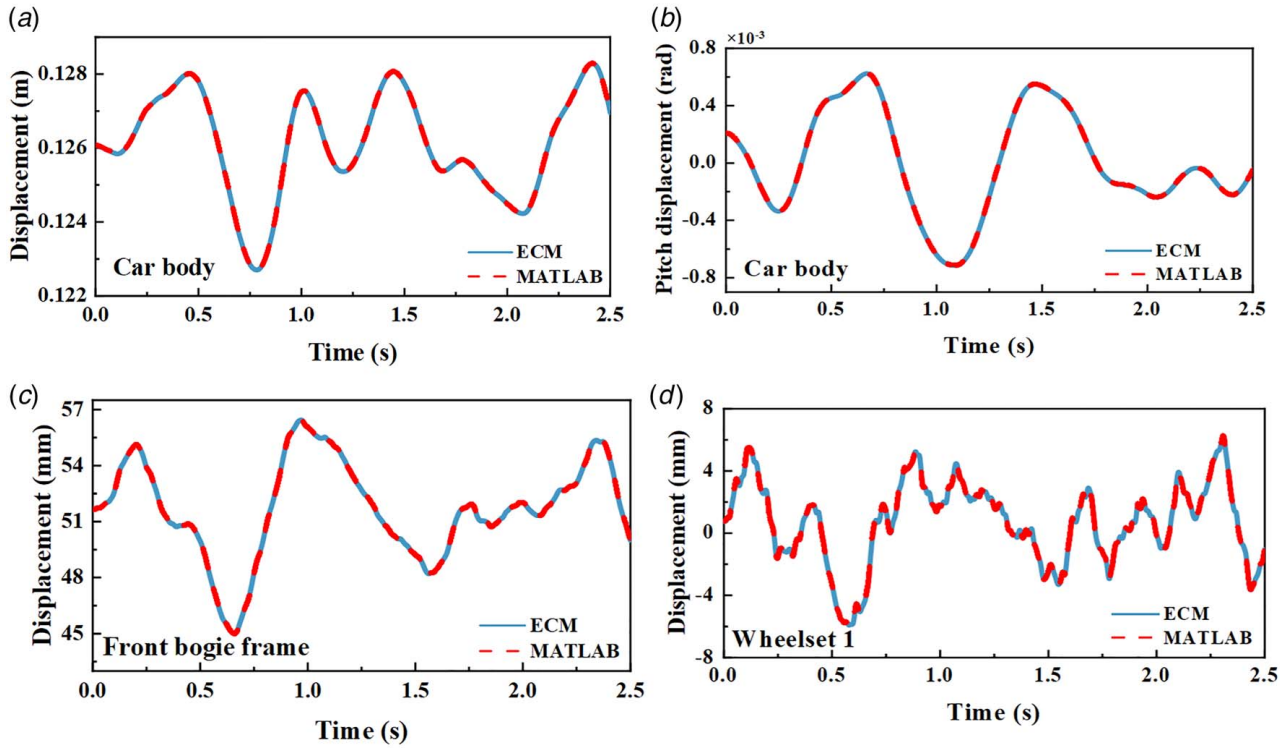

Fig. 5 Validation of the equivalent circuit model of the vehicle

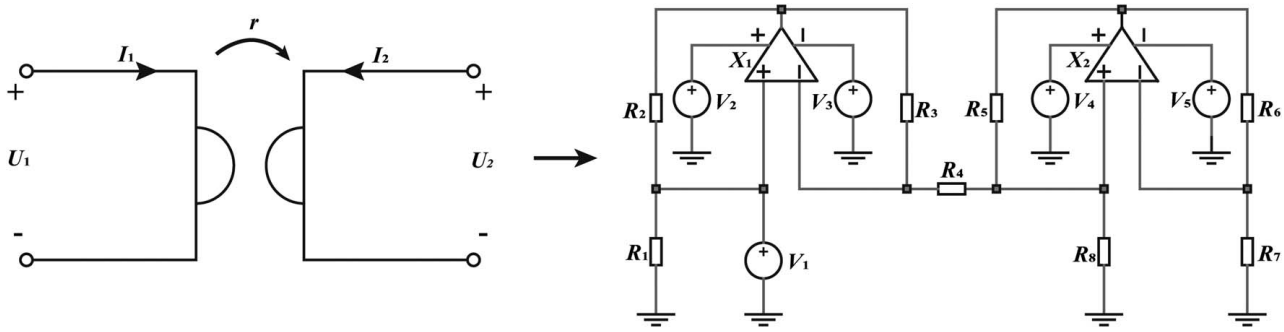

Fig. 6 Schematic diagram and circuit diagram of the gyrator

To verify the established ECM of the vehicle, a MATLAB program based on the Zhai method [38] was developed to compute the dynamic response of each DOF as the vehicle runs on a ballasted track. In the calculation, the parameters of the YZ_{22} passenger car are used, the values are listed in Table 2, and a sixth-order track spectrum is used to generate random track irregularity [38]. Figure 5 presents a comparison of four key parameters: the vertical displacement of the car body, the pitch displacement of the car body, the vertical displacement of the front bogie, and the vertical displacement of wheelset 1. The comparison between the ECM and MATLAB simulation results shows good consistency, confirming that the ECM accurately captures the dynamic behavior of the vehicle subsystems, including the pitch motion of various DOFs.

Furthermore, to incorporate energy harvesters in the ECM, appropriate conversion circuits must be utilized to reflect their coupling nature and behavior. According to the electromechanical coupling equation of a general EMEH (Eq. (11)), the reaction force exerted by the harvester on the vehicle is proportional to the current generated by the harvester. In mechanical–electrical analogies, force corresponds to voltage, indicating that the conversion circuit for an EMEH must preserve the proportionality between the voltage in the vehicle's ECM and the current in the harvester's ECM.

Figure 6 shows the schematic and circuit diagram of a gyrator. Equation (13) provides the theoretical formula that defines the relationship between voltage and current on both sides of the gyrator. U_1 and U_2 represent the input and output voltages,

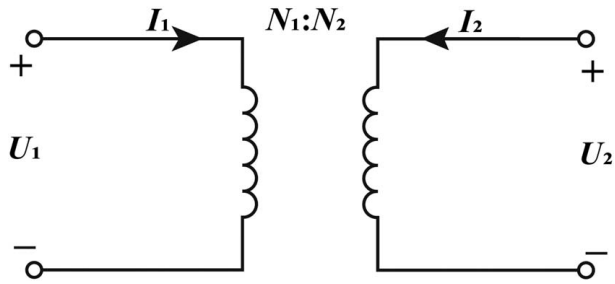

Fig. 7 Schematic diagram of transformer

respectively. I_1 and I_2 denote the currents at the two ports, and r is the gyrator constant. According to its operating principle, a gyrator is a two-port network element that transforms an input voltage at one port into an equivalent output current at the other. This property aligns with the function of the EMEH conversion circuit, making it suitable for integrating the vehicle subsystem and the EMEH subsystem. The gyrator constant r corresponds to the coupling coefficient α of the EMEH [39]:

$$\begin{cases} U_1 = rI_2 \\ U_2 = -rI_1 \end{cases} \tag{13}$$

The gyrator circuit is implemented using two operational amplifiers, five voltage sources, and eight resistances. In this circuit, V_1 represents the input, and the resistance R_8 is the external load. The remaining resistances are identical, all set with a value equal to the coupling coefficient α. Voltage sources V_2 to V_5 provide the necessary power for the two operational amplifiers. When V_1 is fed, virtual shorting occurs in the amplifiers, ensuring that the voltages at the input and output terminals of the operational amplifiers are equal. According to Kirchhoff's law, the relationship between the input voltage V_1 and the current flowing through the load R_8 conforms to Eq. (13). The ratio of these two values corresponds to the electromechanical coupling coefficient α.

Unlike EMEHs, where the reaction force exerted on the vehicle is proportional to the current generated by the harvester, in PEHs, the reaction force is proportional to the voltage. Therefore, a transformer rather than a gyrator is used to ensure proportionality between the voltage in the vehicle's ECM and the PEH. Figure 7 shows a schematic diagram of the transformer, with the primary coil on the left and the secondary coil on the right. The theoretical equation that describes the transformer's behavior is given as follows:

$$\begin{cases} \dfrac{U_1}{U_2} = \dfrac{N_1}{N_2} \\ \dfrac{I_1}{I_2} = \dfrac{N_2}{N_1} \end{cases} \tag{14}$$

In Fig. 7 and Eq. (14), U_1 and U_2 represent the primary and secondary voltages, respectively, while I_1 and I_2 denote the corresponding currents. N_1 and N_2 represent the number of turns in the primary and secondary windings, respectively. When the vehicle subsystem is connected to the primary and the harvester to the secondary, the turns ratio corresponds to the ratio of the voltage in the vehicle's ECM to the voltage generated by the PEH. The relationship between the turns ratio and the PEH's coupling coefficient β is given as $\beta = N_2/N_1$. In SIMETRIX, an ideal transformer component can be directly used to link the vehicle and the PEH subsystem. The reciprocal of the coupling coefficient β corresponds to the transformer's turns ratio.

After integrating the vehicle ECM with the energy harvester (EMEH or PEH), the SMFE and SECE interface circuits can then be shunted accordingly to further boost the power output. In both interface circuits, the switch control is critical. To ensure that the switches operate precisely at the peaks, self-powered circuits with autonomous control have been designed [26,28,29]. The self-powered SMFE (SP-SMFE) interface circuit is shown in Fig. 8.

The SP-SMFE circuit consists of two comparators, two switches, four diodes, one inductor, and two capacitors, with its input terminal connected to EMEH and its output terminal connected to an external load R_3. The two comparators control the switches. When the current flows clockwise, the voltage at the noninverting input of comparator U_1 exceeds that of its inverting input, triggering switch S_1 to close. Simultaneously, the inputs of comparator U_2 are configured oppositely, keeping switch S_2 open. When the current reaches its peak, both switches momentarily open, allowing the energy stored in inductor L_2 to transfer to capacitor C_1. As the current reverses direction and flows counterclockwise, U_2 prompts S_1 to open, and U_1 triggers S_2 to close. Similarly, when the current reaches its negative peak, both switches temporarily open, allowing inductor L_2 to transfer energy to capacitor C_2. The value of L_2 must be significantly larger than the equivalent inductance of the EMEH to reduce the current peak and ensure a rapid current drop to zero when both switches are closed. In this study, L_2 is set to 300 mH, C_1 and C_2 are set to 500 μF, and R_2 is 13 Ω. All other components are ideal elements in the simulation. By integrating the vehicle ECM, the EMEH, and the SMFE interface circuit, the vehicle-EMEH-SMFE coupled model is established, as shown in Fig. 9.

Similarly, a self-powered SECE (SP-SECE) circuit for the PEH is shown in Fig. 10. Before the voltage output of the PEH reaches its peak, the rectified current charges capacitor C_2. During this period, both transistors Q_1 and Q_2 remain nonconductive. At the instant when the voltage across C_1 reaches its peak, the voltage across

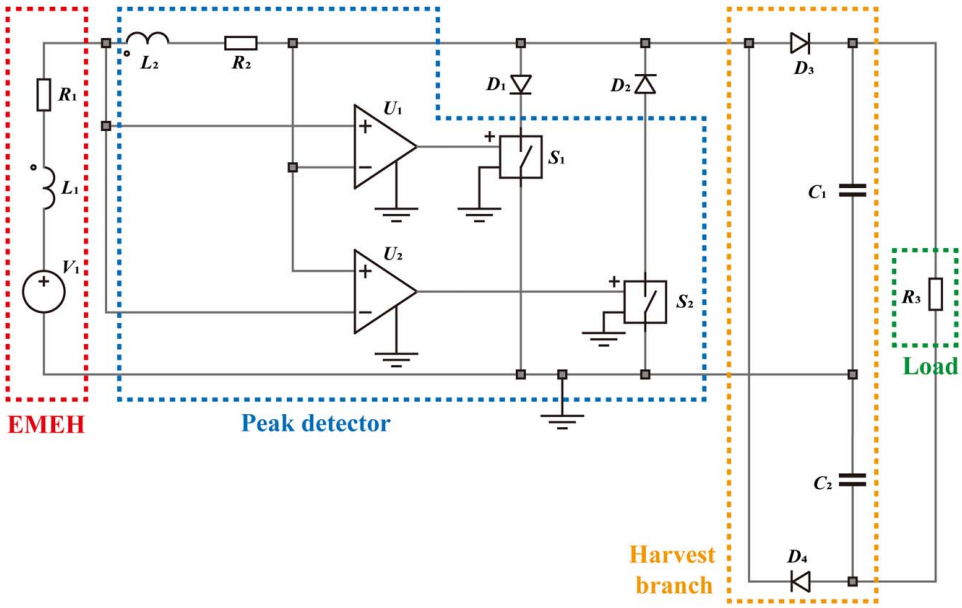

Fig. 8 The schematic of the SP-SMFE interface circuit

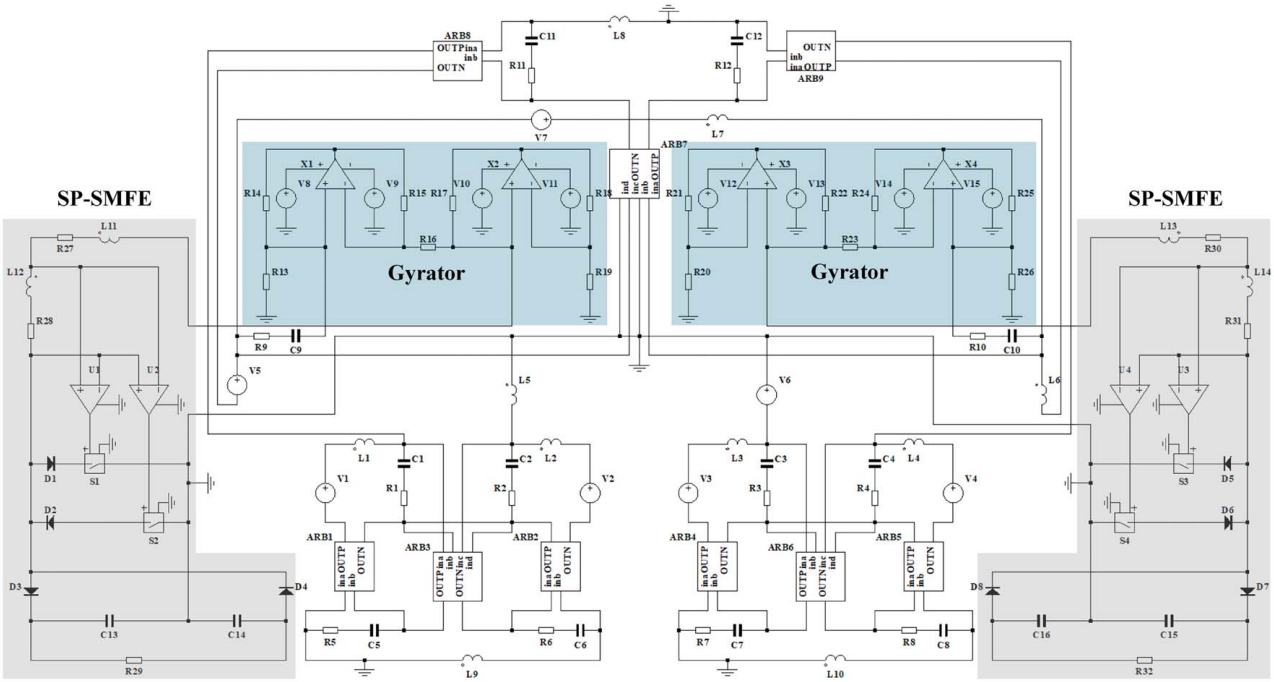

Fig. 9 The circuit schematic of the vehicle-EMEH-SMFE coupled model

C_2 exceeds that on C_1, resulting in a reverse current flowing into the emitter of Q_1. This triggers both transistors (Q_1 and Q_2) to become conductive, allowing the energy stored in C_1 to transfer to inductor L_1. Once the energy transfer is completed, the transistors switch off autonomously, and L_1 starts to supply power to capacitor C_3 and load R_4. The parameters of the circuit components are listed in Table 3.

By integrating the vehicle ECM, the PEH, and the SP-SECE interface circuit, the vehicle-PEH-SECE coupled model is established, as shown in Fig. 11.

4 Analysis of Coupled Dynamics and Energy-Harvesting Performance

Under varying operational conditions, complex excitations affect both the energy harvester's output performance and the vehicle's dynamics. Different excitation types, such as harmonic and random, may influence the energy conversion efficiency and the output characteristics. Moreover, the fluctuations in the energy harvester's output can feed back into the vehicle, exerting a reaction force on the vehicle and impacting overall vehicle dynamic stability. Therefore, understanding the interaction between the energy harvester and the vehicle under different excitation conditions is crucial for optimizing energy harvester design and enhancing vehicle safety and comfort. Meanwhile, in this study, the energy harvesters are modeled as damper-like lumped elements. This simplification allows us to focus on system-level interactions without being constrained by specific device geometries. Regarding the electromechanical coupling coefficients, they were determined in reverse, based on the typical power requirements of commonly used onboard sensor systems, which typically range from 10 to 100 mW [1]. Specifically, the coupling coefficient of the EMEH is set to 100, yielding a nominal power output of approximately 15 mW with a standard interface circuit. The PEH's coupling coefficient is set to 0.0033, resulting in a power output of around 20 mW. This reverse parameter determination ensures that the simulated harvesters operate within a practically useful range, thus allowing us to meaningfully evaluate their impacts on vehicle dynamics under real-world conditions. Given the inherent

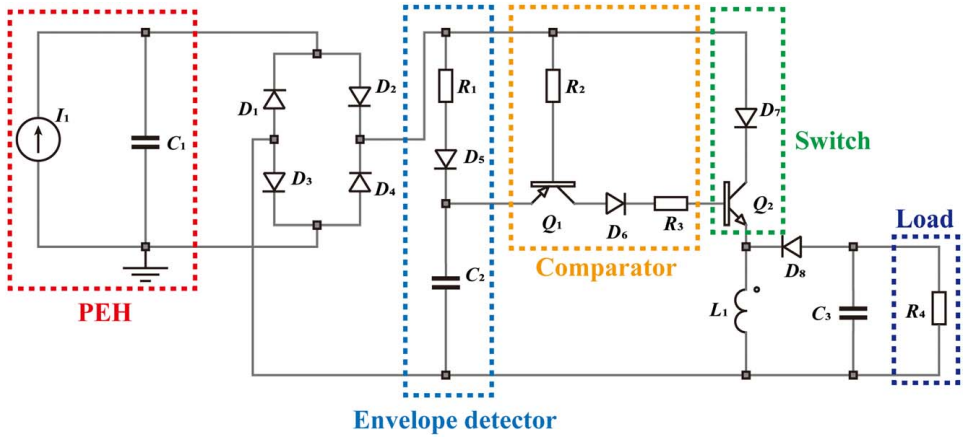

Fig. 10 The schematic of the SP-SECE interface circuit

Table 3 Parameters of SP-SECE interface circuit

Parameter	Type/value
Diode(D_1–D_8)	Ideal model
C_1	180 nF
C_2	2 nF
C_3	10 μF
L_1	470 μH
R_1	200 kΩ
R_2 and R_3	1 kΩ
Q_1	2N2904
Q_2	2N2222

scalability of energy harvesters, this approach remains valid and broadly applicable across various implementation scenarios.

4.1 Analysis of Energy-Harvesting Performance Under Harmonic Excitation. Both the excitation frequency and the external load impact the output of an energy harvester. This section investigates and compares the voltage and power outputs of an EMEH with an SMFE circuit and a PEH with an SECE circuit under varying excitation frequencies and loads against those with a standard circuit. The harmonic force excitation has an offset of 109 kN and a peak-to-peak amplitude of 70 kN. This offset approximately corresponds to the RMS value of the wheel–rail contact force experienced by a YZ_{22} train operating on an irregular track. The standard circuit, which is a simple resistive load widely utilized in prior research, provides a benchmark model for assessing the advantages of the interface circuits in boosting power output.

Figure 12 presents the output characteristics of an EMEH shunted to an SMFE circuit and a standard circuit under different excitation frequencies and load resistances. It is important to note that the wheel–rail forces generated during vehicle operation are predominantly low-frequency [38]. Therefore, a low-frequency excitation range of 1–10 Hz was selected for analysis. In Fig. 12(*a*), it can be observed that as the excitation frequency increases, the power outputs from both circuits first rise and then decrease. With the standard circuit, a maximum power output of 19.73 mW occurs at 4 Hz, while using the SP-SMFE circuit shifts the optimal excitation frequency to 6 Hz and leads to generating a significantly higher maximum power output of 1.33 W. It is noteworthy that vehicle vibration frequencies are primarily concentrated below 10 Hz [38], and within this range, the SP-SMFE circuit consistently outperforms the standard circuit in power output. As the external load resistance increases, as demonstrated in Fig. 12(*b*), the rise in the output voltage of the SP-SMFE circuit is significantly more pronounced than that in the standard circuit. Furthermore, at higher resistance levels, the power output of the SP-SMFE circuit remains nearly constant and consistently higher than that of the standard circuit, whose power output continues to decline. These results indicate that under low-frequency harmonic excitations, the SP-SMFE circuit significantly enhances the power output of the EMEH compared to the standard circuit.

The results for the PEH shunted to an SP-SECE circuit are shown in Fig. 13(*a*). With the integration of the SP-SECE circuit, the optimal excitation frequency of the PEH rises from 2 Hz to 3 Hz. As the frequency increases, both circuits exhibit an initial rise in output voltage and power, followed by a decline. The SP-SECE circuit achieves a maximum power output of 175.90 mW, compared to 52.82 mW of the standard circuit. Moreover, within the frequency range below 10 Hz, the SP-SECE circuit consistently generates higher power output than the standard circuit. As shown in Fig. 13(*b*), as the resistance increases, the output voltage of both circuits gradually increases, but the SP-SECE circuit shows a markedly higher growth rate than the standard circuit. As a result, the power output of the SP-SECE circuit remains nearly constant at approximately 115 mW, consistently exceeding that of the standard circuit and exhibiting greater stability. In contrast, the output power of the stand circuit initially increases and then decreases, reaching a maximum power of 46.15 mW at an optimal resistance of about 300 kΩ. This suggests that integrating the SP-SECE circuit into onboard harvesters can not only boost the power output but also effectively mitigate the load-matching challenge.

The comparison of the two interface circuits reveals that under harmonic excitation, both significantly enhance the energy

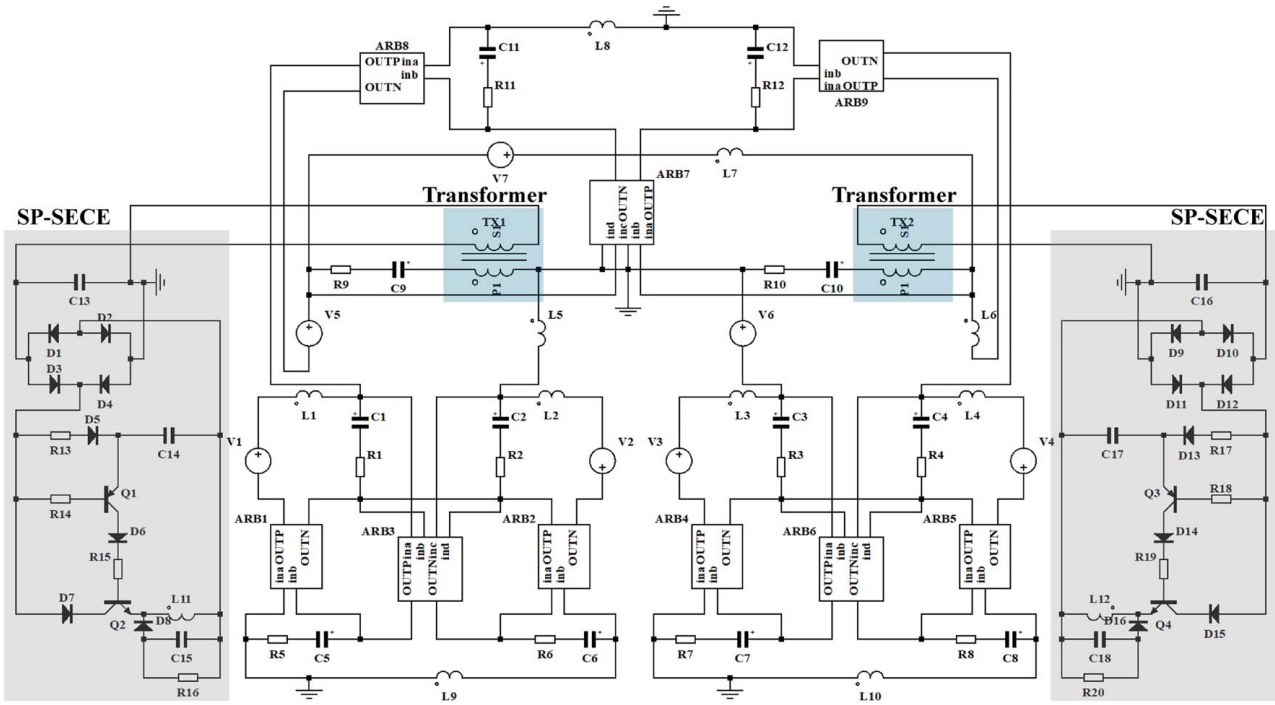

Fig. 11 The circuit schematic of the vehicle-PEH-SECE coupled model

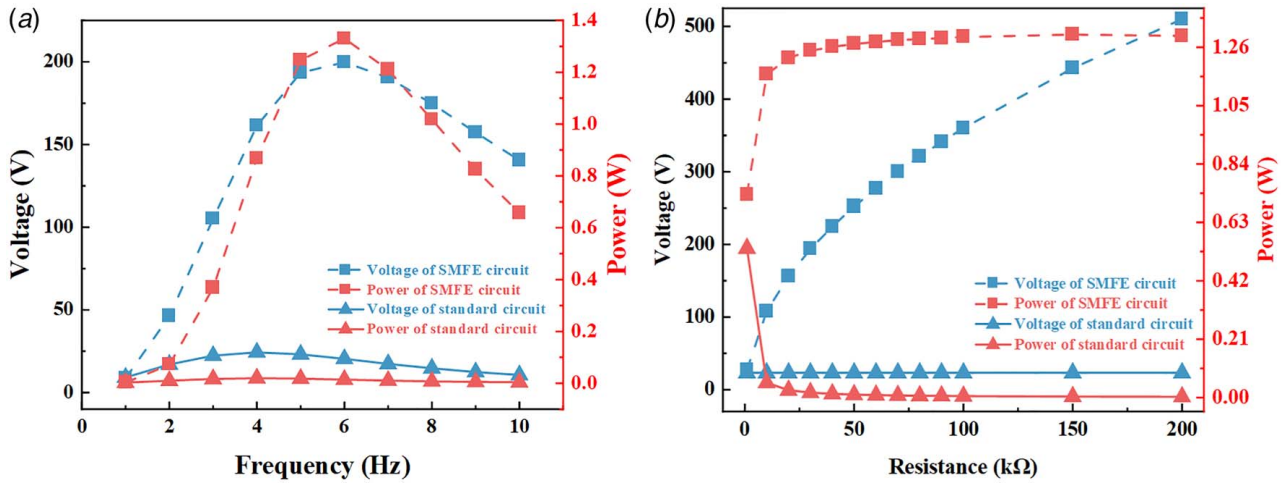

Fig. 12 The output of EMEH under different frequencies and resistances: (*a*) $\alpha = 100$ and $R = 300$ kΩ and (*b*) $\alpha = 100$ and $f = 5$ Hz

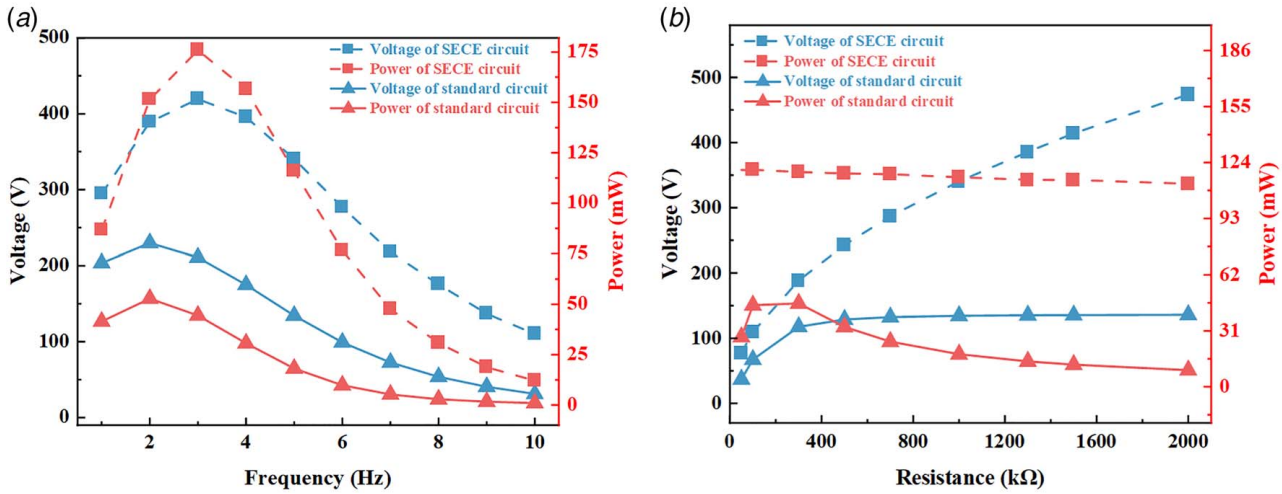

Fig. 13 The output of PEH under different frequencies and resistance: (*a*) $\beta = 0.0033$ and $R = 1000$ kΩ and (*b*) $\beta = 0.0033$ and $f = 5$ Hz

harvester's power output while slightly increasing the optimal excitation frequency. However, this frequency shift may lead to a deviation from the original design intent, resulting in a mismatch with the vibration characteristics of the vehicle. Therefore, future efforts should be devoted to developing and optimizing interface circuits to better align the optimal excitation frequency with real-world vehicle conditions, ensuring improved compatibility and efficiency.

4.2 Influence of Energy Harvester on Vehicle Dynamics Under Harmonic Excitation. Due to the coupling effects, introducing the interface circuits may also change the reaction force exerted on the vehicle by the energy harvesters. To investigate the impact of the harvester installation on the vehicle dynamics, the bogie frame response is analyzed under varying load frequencies and external loads.

Figure 14 compares the bogie frame velocity under three conditions: (1) with the EMEH installed and connected to an SP-SMFE interface circuit, (2) with the EMEH installed and connected to a standard circuit, and (3) without the EMEH installed. As shown in Fig. 14, compared to the case without the EMEH, the installation of the EMEH with an SP-SMFE circuit reduces the bogie frame velocity. When the SP-SMFE circuit is installed, the velocity discrepancy initially increases and then decreases as the excitation frequency increases. At lower frequencies (2–4 Hz), the discrepancy is more pronounced, reaching up to −0.24%. In contrast, the discrepancy caused by the standard circuit remains nearly constant and never exceeds −0.0023%. Regardless of excitation frequency and external load, the velocity discrepancy induced by the SP-SMFE interface circuit is consistently greater than that of the standard circuit. This suggests that the interface circuit amplifies variation in the vehicle's dynamic response during operation, with these discrepancies being more pronounced at lower excitation frequencies.

The bogie frame responses after installing the PEH are shown in Fig. 15. There is no significant variation between the cases with the SP-SECE circuit and with the standard circuit. The velocity discrepancy is relatively large in the low-frequency range (1–3 Hz), but it gradually decreases to almost zero as the frequency increases. Compared to the case with an SP-SECE circuit, the case with the standard circuit exhibits a smaller velocity discrepancy across most of the frequency range. When the excitation frequency exceeds 6 Hz, the velocity discrepancies caused by the standard and SP-SECE circuits gradually decrease and approach zero. Furthermore, regardless of the external load, the velocity of the bogie frame remains highly stable in the cases of using the SP-SECE and standard circuits. While the SP-SECE interface circuit has a slightly greater impact on the dynamics of the bogie frame than

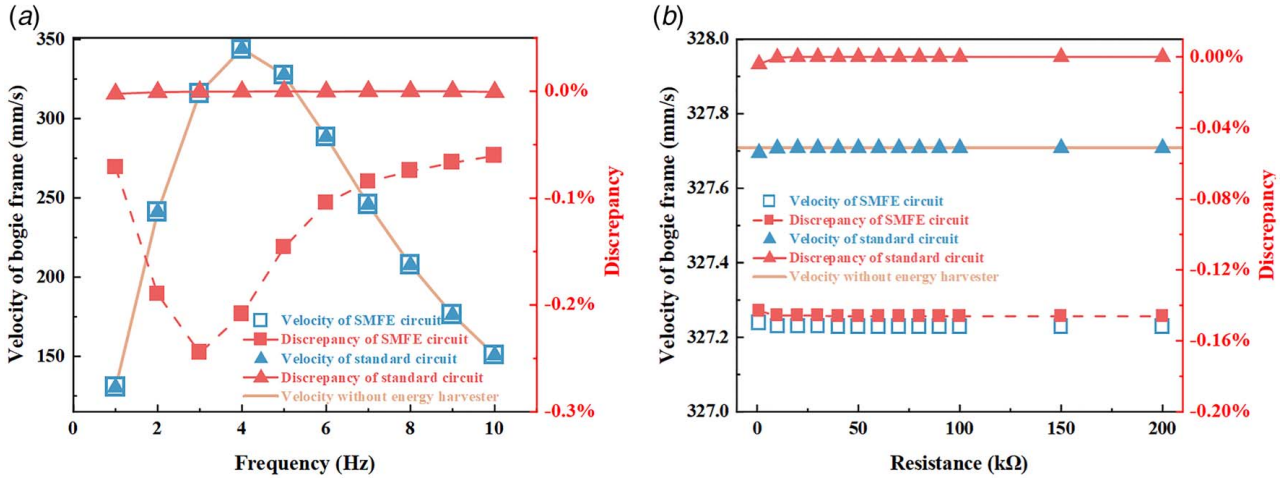

Fig. 14 Velocity and discrepancy of bogie frame after installing EMEH: (*a*) $\alpha = 100$ and $R = 300$ kΩ and (*b*) $\alpha = 100$ and $f = 5$ Hz (discrepancy = data after energy harvester installation − data without energy harvester/Data without energy harvester)

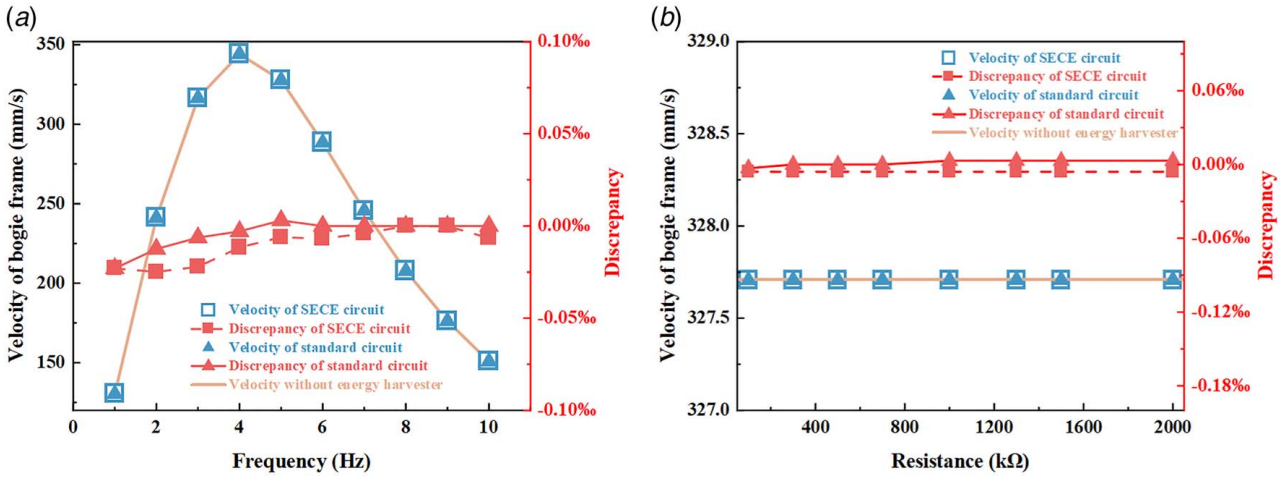

Fig. 15 Velocity and discrepancy of bogie frame after installation PEH: (*a*) $\beta = 0.0033$ and $R = 1000$ kΩ and (*b*) $\beta = 0.0033$ and $f = 5$ Hz

the standard circuit, the discrepancy caused is minimal. This suggests that the external load resistance has a negligible effect on the bogie frame.

The above results show that, while the influences of the energy harvesters (EMEHs and PEHs) on vehicle dynamics are small regardless of the interface circuits, the overall discrepancy induced by the power-boosting interface circuits (SP-SMFE and SP-SECE) is generally larger than that induced by the standard circuit. Therefore, to ensure vehicle safety and comfort, it is crucial to account for the potential impacts of interface circuits on vehicle dynamic responses when designing/installing onboard energy harvesters. It becomes even more critical as harvester size increases because the resulting negative effects can become more significant.

4.3 Analysis of Energy Harvester Performance Under Wheel–Rail Force Excitation. In the previous two sections, we primarily focused on investigating the harvester's output performance and its impact on the vehicle under harmonic excitations. However, harmonic excitations only reflect idealized conditions and cannot represent the complex excitation a vehicle experiences during real-world operation. This section advances the research by replacing harmonic excitation with wheel–rail force excitation calculated using the Zhai method [38]. To simulate random track irregularities, the power spectral density (PSD) of the U.S. Federal Railroad Administration (FRA) sixth class track is adopted. In this section, the train speed is set to 140 km/h, which remains within the maximum speed allowed by the six-grade track spectrum and complies with the standard. The expression

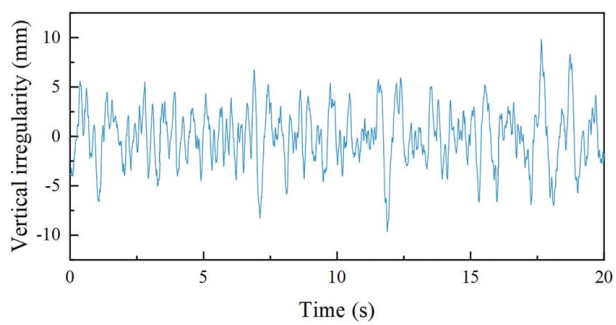

Fig. 16 Track vertical irregularity derived from inverse Fourier transformation of the PSD model and adopted in the numerical simulation

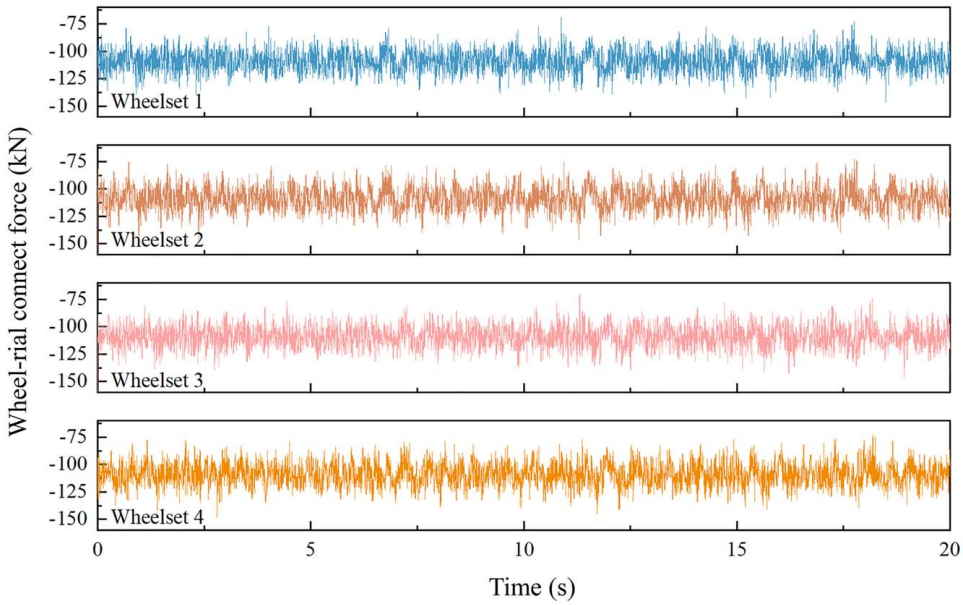

Fig. 17 The calculated wheel–rail contact forces

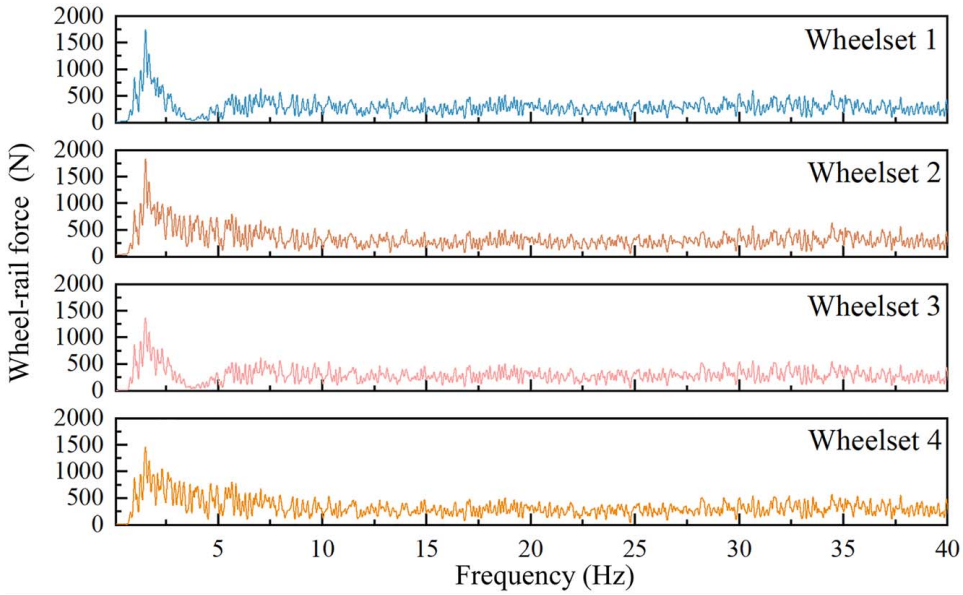

Fig. 18 Corresponding frequency spectra of the wheel–rail contact forces

for this spectrum is given as follows:

$$S_v(\phi) = \frac{A_v \phi_{v2}^2 (\phi^2 + \phi_{v1}^2)}{\phi^4 (\phi^2 + \phi_{v2}^2)} \tag{15}$$

where $S_v(\phi)$ is the power spectral density of track height irregularities, ϕ is the spatial frequency of the irregularities, A_v is the roughness constant, and ϕ_{v1} and ϕ_{v2} are the cutoff frequencies. To facilitate numerical simulation, the track irregularity PSD is converted into time-domain samples. This is achieved by performing an inverse Fourier transform on Eq. (15). An example of the resulting time-domain signal is shown in Fig. 16.

The corresponding forces are illustrated in Figs. 17 and 18. As shown in the figures, the wheel–rail forces range from 75 kN to 140 kN, with their frequency content primarily concentrated below 5 Hz within the frequency range of interest. These forces more accurately represent real-world conditions and enable a more realistic simulation of vehicle dynamics on irregular railway tracks.

The voltage outputs from the two EMEHs under the wheel–rail force excitation are presented in Fig. 19. The results show that the voltage outputs of the EMEHs exhibit irregular fluctuations caused by track irregularities that generate random variations in the wheel–rail force. As shown in Fig. 19(*a*), when the SP-SMFE interface circuit is connected, the voltage outputs from the two EMEHs remain relatively stable, with the fluctuation amplitude staying around 10 V, indicating consistent output performance. The RMS power outputs are 3.388 mW and 3.715 mW, respectively. In contrast, with the standard circuit (Fig. 19(*b*)), the output voltage varies significantly between −10 V and 10 V, and the RMS power outputs are between 0.886 mW and 1.126 mW. The fluctuation amplitude is markedly larger than that observed in

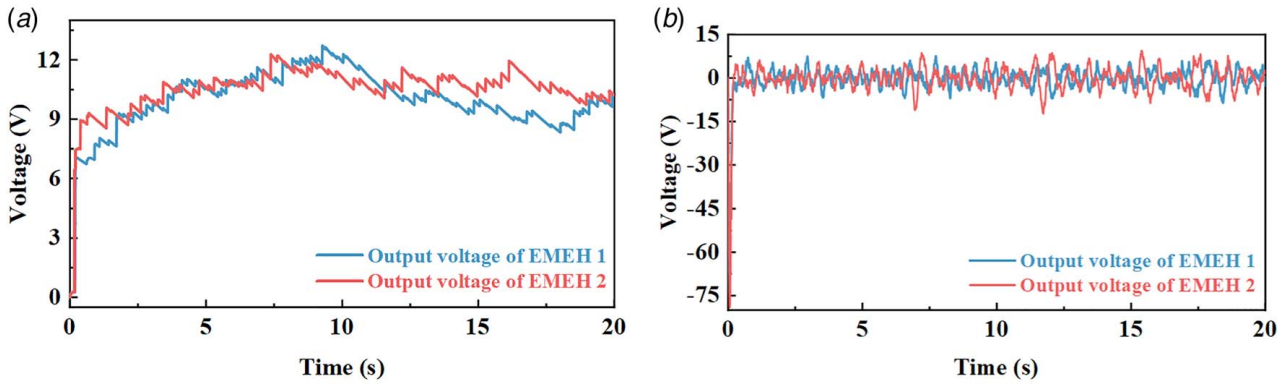

Fig. 19 The output of EMEH under wheel–rail force excitation: (*a*) output voltage after SP-SMFE circuit installation and (*b*) output voltage after standard circuit installation

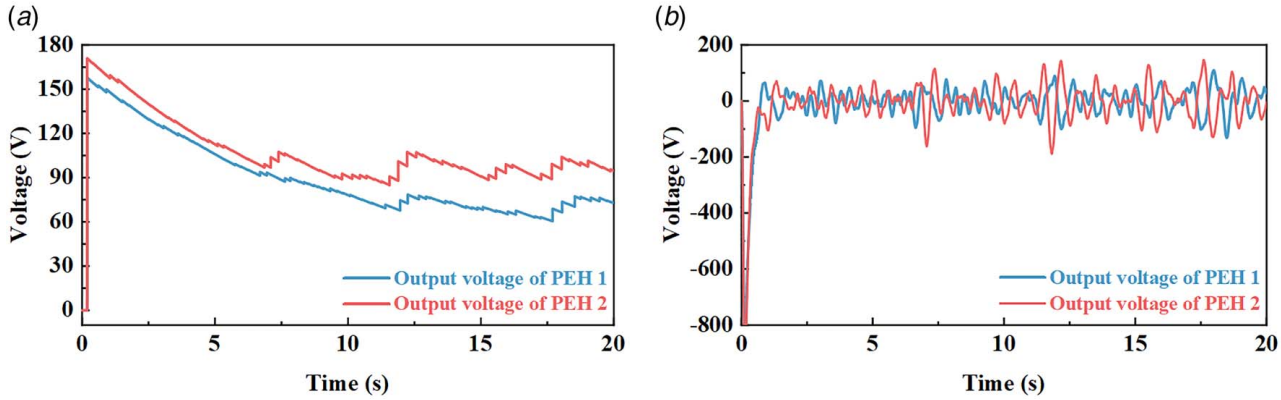

Fig. 20 The output of PEH under wheel–rail force excitation: (*a*) output voltage after SP-SECE circuit installation and (*b*) output voltage after standard circuit installation

the SP-SMFE circuit. Such severe voltage fluctuations may easily impair the normal operation of subsequent power supply equipment.

When PEHs are subjected to wheel–rail force excitation, their voltage outputs also exhibit irregular fluctuations. As shown in Fig. 20, similar to the EMEH case, after connecting the SP-SECE circuit, the voltage output becomes more stable, maintaining a relatively stable value of approximately 90 V. The RMS power outputs are 8.729 mW and 11.908 mW, respectively. In contrast, with the standard circuit, the voltage varies dramatically between −100 V and 100 V; the two energy harvesters' RMS power outputs are 8.226 mW and 9.801 mW, respectively. Although the stable voltage after connecting the SP-SECE circuit is lower than that delivered by the standard circuit, the electrical output stability is greatly improved, and the RMS power output is higher. This highlights the crucial role of interface circuits in enhancing the output performance of the energy harvesters.

Integrating both interface circuits can significantly enhance the output stability and RMS power outputs of the two types of energy harvesters, with the SP-SECE and SP-SMFE circuits exhibiting much more stable performance under random wheel–rail force excitation and reduced fluctuations compared to the standard circuit. This stability is vital for power supply under real-world operational conditions, especially in ensuring a stable power supply for critical equipment like structural health monitoring sensors in vehicles. These vehicle-level analysis results, derived from the established coupled model in this study, indicate that utilizing SP-SECE and SP-SMFE circuits effectively enhances the performance of the energy harvesters, making them more adaptable to the complex, random load environments and improving their practicality and reliability in rail transportation.

5 Conclusion

This study establishes an ECM that integrates vehicle dynamics with onboard energy harvesters and power-boosting interface circuits, aiming to systematically evaluate the energy harvesters' power generation performance and their dynamic interactions with vehicle systems postinstallation. Through parametric analysis under various excitation conditions, three main conclusions are obtained and summarized as follows:

(1) Under harmonic excitations, as both excitation frequency and load resistance increase, energy harvesters connected to power-boosting interface circuits demonstrate significantly enhanced power output compared to those connected to standard circuits. For the same EMEH, the SMFE circuit produces a maximum power output of 1.33 W at 6 Hz, which is much higher than 19.73 mW produced by a standard circuit at 4 Hz. Similarly, for the PEH, the SECE circuit consistently generates a higher power output than the standard circuit. The maximum power output with the SECE circuit is 175.90 mW at 3 Hz, whereas the standard circuit produces only 52.82 mW at 2 Hz.

(2) For both the EMEH and PEH connected to power-boosting interface circuits, their impacts on vehicle dynamics are more pronounced. The maximum discrepancy in the bogie frame's velocity reaches −0.24% for the EMEH with the

SMFE circuit and −0.02% for the PEH with the SECE circuit. In contrast, when using the standard circuit, the impacts on vehicle dynamics remain negligible.

(3) Under wheel–rail force excitation, the voltage outputs from energy harvesters exhibit irregular fluctuations, and the RMS power output remains higher when using power-boosting interface circuits. For the EMEH, integrating the SMFE circuit leads to the generation of an RMS power of 3.715 mW, compared to only 0.886 mW with the standard circuit. For the PEH, the SECE circuit achieves a maximum RMS power of 11.908 mW, whereas the standard circuit produces 9.801 mW only. The power-boosting interface circuits can substantially enhance the power-generating capacity in real-world excitation conditions.

Funding Data

- The National Natural Science Foundation of China (52305135).
- The Guangdong Provincial Project (2023QN10L545).
- The Guangzhou Municipal Science and Technology Bureau (SL2023A03J00869 and SL2023A04J01741).
- The Guangdong Provincial Key Lab of Integrated Communication, Sensing and Computation for Ubiquitous Internet of Things (2023B1212010007).
- The Guangzhou Municipal Key Laboratory on Future Networked Systems (024A03J0623).
- The Technology Development Project (XYZX040401).

Conflict of Interest

There are no conflicts of interest.

Data Availability Statement

The datasets generated and supporting the findings of this article are obtainable from the corresponding author upon reasonable request.

Nomenclature

v = Vehicle speed
l_c = Half of rolling stock axle spacing
l_t = Half of wheel base
p_i = Wheel–rail contact force
D_{pz} = Primary vertical damping
D_{sz} = Secondary vertical damping
F_{EH} = Reaction force of energy harvester
F_{0i} = Self-excitation force
J_c = Vehicle roll moment of inertia
J_t = Bogie roll moment of inertia
K_{pz} = Primary vertical stiffness
K_{sz} = Secondary vertical stiffness
M_c = Mass of car body
M_t = Mass of bogie
M_w = Mass of wheelset
Z_c = Vertical motion of car body
Z_{ti} = Vertical motion of bogie
Z_{wi} = Vertical motion of wheelset
β_c = Pitch motion of car body
β_{ti} = Pitch motion of bogie

References

[1] Hodge, V. J., O'Keefe, S., Weeks, M., and Moulds, A., 2015, "Wireless Sensor Networks for Condition Monitoring in the Railway Industry: A Survey," IEEE Trans. Intell. Transp. Syst., **16**(3), pp. 1088–1106.

[2] Bernal, E., Spiryagin, M., and Cole, C., 2019, "Onboard Condition Monitoring Sensors, Systems and Techniques for Freight Railway Vehicles: A Review," IEEE Sens. J., **19**(1), pp. 4–24.

[3] Hosseinkhani, A., Younesian, D., Eghbali, P., Moayedizadeh, A., and Fassih, A., 2021, "Sound and Vibration Energy Harvesting for Railway Applications: A Review on Linear and Nonlinear Techniques," Energy Rep., **7**, pp. 852–874.

[4] De Oliveira, R. H., Loprencipe, G., Vaz De Almeida Filho, F. G., and De Sousa Pissardini, R., 2022, "Experimental Investigation on the Use of Multiple Very Low-Cost Inertial-Based Devices for Comfort Assessment and Rail Track Monitoring," Measurement, **199**, p. 111549.

[5] Tang, H., Kong, L., Fang, Z., Zhang, Z., Zhou, J., Chen, H., Sun, J., and Zou, X., 2024, "Sustainable and Smart Rail Transit Based on Advanced Self-Powered Sensing Technology," iScience, **27**(12), p. 111306.

[6] Hou, W., Li, Y., Zheng, Y., and Guo, W., 2020, "Multi-Frequency Energy Harvesting Method for Vehicle Induced Vibration of Rail Transit Continuous Rigid Bridges," J. Clean. Prod., **254**, p. 119981.

[7] Mousavi, M., Ziaei-Rad, S., and Karimi, A. H., 2023, "Piezoelectric-Based Energy Harvesting From Bridge Vibrations Subjected to Moving Successive Vehicles by Functionally Graded Cantilever Beams—Theoretical and Experimental Investigations," Mech. Syst. Signal Process., **188**, p. 110015.

[8] Guo, Z., Jiang, S., Shen, Y., Jiang, G., Xiao, B., Xu, Q., and Li, M., 2025, "Nonlinear Dynamic Analysis and Vibration Reduction of Two Sandwich Beams Connected by a Joint With Clearance," Mech. Syst. Signal Process., **223**, p. 111828.

[9] Madan, A., Zhao, C., Han, C., Dong, Y., and Yang, Y., 2025, "Monitoring Rail Track Bolt Loosening Using Fiber-Optic Distributed Acoustic Sensing," Sens. Actuators A: Phys., **382**, p. 116176.

[10] Li, P., Wang, M., Yu, T., Feng, N., Lan, C., Yang, K., Li, S., and Zhang, H., 2024, "A Monitoring Method of Rail Fastener Reaction Force Based on Iron Pad Strain," Constr. Build. Mater., **418**, p. 135169.

[11] Li, C., Luo, S., Cole, C., and Spiryagin, M., 2017, "An Overview: Modern Techniques for Railway Vehicle On-Board Health Monitoring Systems," Veh. Syst. Dyn., **55**(7), pp. 1045–1070.

[12] Xie, X. D., and Wang, Q., 2015, "Energy Harvesting From a Vehicle Suspension System," Energy, **86**, pp. 385–392.

[13] Pan, Y., Liu, F., Jiang, R., Tu, Z., and Zuo, L., 2019, "Modeling and Onboard Test of an Electromagnetic Energy Harvester for Railway Cars," Appl. Energy, **250**, pp. 568–581.

[14] Abdelkareem, M. A. A., Xu, L., Ali, M. K. A., Elagouz, A., Mi, J., Guo, S., Liu, Y., and Zuo, L., 2018, "Vibration Energy Harvesting in Automotive Suspension System: A Detailed Review," Appl. Energy, **229**, pp. 672–699.

[15] Wang, R., Allen, P., Song, Y., and Wang, Z., 2022, "Modelling and Analysis of Power-Regenerating Potential for High-Speed Train Suspensions," Sustainability, **14**(5), p. 2542.

[16] Lombardi, G., and Lallart, M., 2021, "Synchronous Electric Charge and Induced Current Extraction (SECICE): A Unified Nonlinear Technique Combining Piezoelectric and Electromagnetic Harvesting," Smart Mater. Struct., **30**(2), p. 025029.

[17] Wang, S., Peng, W., Kong, W., Luo, D., Zhang, Z., and Li, L., 2023, "An Energy Harvesting Shock Absorber for Powering On-Board Electrical Equipment in Freight Trains," iScience, **26**(9), p. 107547.

[18] Liu, Y., Xu, L., and Zuo, L., 2017, "Design, Modeling, Lab, and Field Tests of a Mechanical-Motion-Rectifier-Based Energy Harvester Using a Ball-Screw Mechanism," IEEE/ASME Trans. Mechatron., **22**(5), pp. 1933–1943.

[19] Li, Y., Xie, C., Quan, S., Zen, C., and Li, W., 2018, "Vibration Energy Harvesting in Vehicles by Gear Segmentation and a Virtual Displacement Filtering Algorithm," Int. J. Energy Res., **42**(4), pp. 1387–1786.

[20] Izhar, Iqbal, M., and Khan, F., 2023, "Hybrid Acoustic, Vibration, and Wind Energy Harvester Using Piezoelectric Transduction for Self-Powered Wireless Sensor Node Applications," Energy Convers. Manage., **277**, p. 116635.

[21] Wang, Z., Wang, W., Tang, L., Tian, R., Wang, C., Zhang, Q., Liu, C., Gu, F., and Ball, A. D., 2022, "A Piezoelectric Energy Harvester for Freight Train Condition Monitoring System With the Hybrid Nonlinear Mechanism," Mech. Syst. Signal Process., **180**, p. 109403.

[22] Lopes, M. V., Eckert, J. J., Martins, T. S., et al., 2020, "Optimizing Strain Energy Extraction From Multi-Beam Piezoelectric Devices for Heavy Haul Freight Cars," J. Braz. Soc. Mech. Sci. Eng., **42**(1), p. 59.

[23] Jung, I., Choi, J., Park, H.-J., Lee, T.-G., Nahm, S., Song, H.-C., Kim, S., and Kang, C.-Y., 2020, "Design Principles for Coupled Piezoelectric and Electromagnetic Hybrid Energy Harvesters for Autonomous Sensor Systems," Nano Energy, **75**, p. 104921.

[24] Lefeuvre, E., Badel, A., Richard, C., and Guyomar, D., 2005, "Piezoelectric Energy Harvesting Device Optimization by Synchronous Electric Charge Extraction," J. Intell. Mater. Syst. Struct., **16**(10), pp. 865–876.

[25] Zhang, Z., Xiang, H., Tang, L., and Yang, W., 2023, "A Comprehensive Analysis of Piezoelectric Energy Harvesting From Bridge Vibrations," J. Phys. D: Appl. Phys., **56**(1), p. 014001.

[26] Zhang, Z., Xiang, H., and Tang, L., 2021, "Modeling, Analysis and Comparison of Four Charging Interface Circuits for Piezoelectric Energy Harvesting," Mech. Syst. Signal Process., **152**, p. 107476.

[27] Arroyo, E., and Badel, A., 2011, "Electromagnetic Vibration Energy Harvesting Device Optimization by Synchronous Energy Extraction," Sens. Actuators A: Phys., **171**(2), pp. 266–273.

[28] Jia, S., Zeng, C., Shi, G., Hong, C., Han, J., and Xia, Y., 2023, "A Self-Powered Synchronous Magnetic Flux Extraction Interface for Electromagnetic Energy Harvesting," Microelectron. J., **140**, p. 105943.

[29] Xie, Z., Teng, L., Wang, H., Liu, Y., Fu, M., and Liang, J., 2023, "A Self-Powered Synchronous Switch Energy Extraction Circuit for Electromagnetic Energy Harvesting Enhancement," IEEE Trans. Power Electron., **38**(8), pp. 9972–9982.

[30] Qiu, J., Wang, H., Liu, Y., Fu, M., et al.et al., 2024, "A Synchronous Current Inversion and Energy Extraction Circuit for Electromagnetic Energy Harvesting Enhancement," IEEE Trans. Circuits Syst. Regul. Pap., **71**(12), pp. 5471–5481.
[31] Pan, Y., Guo, S. J., Jiang, R.J, Xu, Y., Tu, Z. W., and Zuo, L., 2018, "Performance Evaluation of Train Suspension Energy Harvesting Shock Absorber on Railway Vehicle Dynamics," Proceedings of the ASME 2018 Dynamic Systems and Control Conference, Atlanta, GA, Sept. 30–Oct. 3.
[32] Du, C., Wang, J., Cao, Y., Xiang, H., Liang, J., Li, X., and Tang, L., 2025, "Performance Enhancement of Piezoelectric Smart Backing Ring (PSBR) Considering the Effect of Installation on the Dynamics of Vehicle-Floating Slab Track Systems," J. Intell. Mater. Syst. Struct., **36**(3), pp. 194–219.
[33] Dziadak, B., Kucharek, M., and Starzyński, J., 2022, "Powering the WSN Node for Monitoring Rail Car Parameters, Using a Piezoelectric Energy Harvester," Energies, **15**(5), p. 1641.
[34] Wang, R., and Wang, Z., 2020, "Evaluation of Power Regeneration in Primary Suspension for a Railway Vehicle," Front. Mech. Eng., **15**(2), pp. 265–278.
[35] Ortiz, J., Monje, P. M., Zabala, N., Arsuaga, M., Etxaniz, J., Aranguren, G., 2014, "New Proposal for Bogie-Mounted Sensors Using Energy Harvesting and Wireless Communications," Proc. Inst. Mech. Eng., Part F: J. Rail Rapid Transit, **228**(7), pp. 807–820.
[36] Li, L. F., Li, J. T., Luo, D. B., Zhang, Z. T., Zeng, K., and Chen, S. Q., 2024, "A Piezo-Electromagnetic Hybrid Multi-Directional Vibration Energy Harvester in Freight Trains," Sustain. Mater. Technol., **41**, p. e00989.
[37] Tang, M., Cao, H., Kong, L., Azam, A., Luo, D., Pan, Y., and Zhang, Z., 2022, "A Hybrid Kinetic Energy Harvester for Applications in Electric Driverless Buses," Int. J. Mech. Sci., **223**, p. 107317.
[38] Zhai, W., 2020, *Vehicle–Track Coupled Dynamics: Theory and Applications*, Springer Singapore, Singapore.
[39] Cheng, S., Wang, N., and Arnold, D. P., 2007, "Modeling of Magnetic Vibrational Energy Harvesters Using Equivalent Circuit Representations," J. Micromech. Microeng., **17**(11), pp. 2328–2335.